Constraints imply limited future weakening of Atlantic meridional overturning circulation

David Bonan
dbonan@caltech.edu

California Institute of Technology https://orcid.org/0000-0003-3867-6009
Andrew Thompson
California Institute of Technology https://orcid.org/0000-0003-0322-4811
Tapio Schneider
California Institute of Technology https://orcid.org/0000-0001-5687-2287
Laure Zanna
New York University
Kyle Armour
University of Washington https://orcid.org/0000-0002-6833-5179
Shantong Sun
Laoshan Laboratory

Article

Keywords:

Posted Date: June 10th, 2024

DOI: https://doi.org/10.21203/rs.3.rs-4456168/v1

Additional Declarations: There is **NO** Competing Interest.

Constraints imply limited future weakening of Atlantic meridional overturning circulation

David B. Bonan[1], Andrew F. Thompson[1], Tapio Schneider[1], Laure Zanna[2], Kyle C. Armour[3,4], Shantong Sun[5]

[1]*Environmental Science and Engineering, California Institute of Technology, Pasadena, California, USA*

[2]*Courant Institute of Mathematical Sciences, New York University, New York City, New York, USA*

[3]*Department of Atmospheric Sciences, University of Washington, Seattle, Washington, USA*

[4]*School of Oceanography, University of Washington, Seattle, Washington, USA*

[5]*Laoshan Laboratory, Qingdao, China*

Climate models simulate a large spread in the projected weakening of the Atlantic meridional overturning circulation (AMOC) over the 21st century. Here, we demonstrate that this uncertainty can be substantially reduced by using a thermal-wind expression that relates the AMOC strength to the meridional density difference and the overturning depth in the Atlantic basin. This expression captures the intermodel spread in AMOC weakening across climate models, with the majority of the intermodel spread arising from overturning depth changes. The overturning depth also establishes a crucial link between the present-day and future AMOC strength. Climate models with a deeper present-day overturning tend to predict greater shoaling under warming. This occurs because their present-day North Atlantic is less stratified, allowing for a deeper penetration of surface buoyancy flux changes, greater density changes at depth, and, consequently, greater AMOC weakening. By integrating observational constraints, we conclude that, regardless of the emission scenario, the AMOC will only experience modest weakening of about 4 Sv by the end of this century. These results indicate that the uncertainty in 21st-century AMOC weakening, and a propensity to predict strong AMOC weakening, can be primarily attributed to climate model biases in accurately simulating the present-day ocean stratification.

State-of-the-art global climate models (GCMs) consistently predict that the Atlantic meridional overturning circulation (AMOC) will weaken in response to rising greenhouse gas concentrations over the 21st century[1–4]. This weakening is important because the AMOC plays a crucial role in ventilating the upper 2000 m of the ocean[5] and transporting heat northward throughout the Atlantic Ocean[6]. These processes regulate Atlantic sea-surface temperatures, which in turn have wide-ranging impacts on regional climates over North America and Western Europe[7,8], Arctic sea-ice variability[9,10], and the location of tropical precipitation[11–13]. Moreover, changes in the AMOC strength are expected to strongly influence regional sea level rise[14–16] and regional climate change[17–19] over the 21st century.

While GCMs consistently predict 21st-century AMOC weakening, there is significant intermodel spread in the rate and magnitude of this weakening, adding considerable uncertainty to future climate projections. For instance, GCMs participating in Phase 6 of the Coupled Model Intercomparison Project (CMIP6)[20] on average predict that, by the end of the century, the AMOC will weaken by about 8 Sv (1 Sv $\equiv 10^6$ m^3 s^{-1}; black line, Fig. 1). However, some GCMs predict that the AMOC will weaken by as little as 2 Sv, while others predict that it will weaken by as much as 15 Sv (Fig. 1). Interestingly, the magnitude of AMOC weakening depends more on the individual GCM considered than on the emission scenario (Fig. 1).

How does the intermodel spread in AMOC projections arise? Over the past few decades, a series of studies have identified a strong correlation between the present-day AMOC strength and AMOC weakening under warming[4,21–26]. In particular, GCMs with a stronger present-day AMOC exhibit greater AMOC weakening. Indeed, the CMIP6 GCMs with the strongest present-day (1981–2010) AMOC tend to exhibit the most AMOC weakening, predicting a decrease of 10–15 Sv by the end of the 21st century (red lines and bars, Fig. 1d). Similarly, the CMIP6 GCMs with the weakest present-day AMOC tend to exhibit the least AMOC weakening, predicting a decrease of 3–6 Sv by the end of the 21st century (blue lines and bars, Fig. 1d).

This implies that the observed AMOC strength can be used to estimate the magnitude of AMOC weakening expected in the 21st century via a so-called ‘emergent constraint,’ which describes a statistical relationship between aspects of the present-day climate and future changes across GCMs. When combined with observations, emergent constraints can be used to reduce uncertainty in future climate projections.

Leveraging any emergent constraint to reduce uncertainty in future climate projections, however, requires a solid understanding of the underlying mechanisms on which the constraint depends[27]. In this case, the mechanisms underpinning the correlation between the present-day AMOC strength and future AMOC weakening remain unclear. It has been suggested that the present-day AMOC relates to AMOC weakening under warming through subsurface stratification in the Labrador Sea, as GCMs with weaker present-day Labrador Sea stratification tend to show greater AMOC weakening[26]. Yet, this explanation for AMOC weakening remains unclear as the Labrador Sea makes a limited contribution to dense water formation in most GCMs[28]. A better understanding of the relationship between the present-day AMOC and its projected changes is necessary to constrain 21st-century AMOC projections.

Here, we present a physical mechanism that explains the relationship between the present-day and future AMOC strength. The mechanism is rooted in thermal-wind balance, which relates the AMOC strength to the meridional density difference and overturning depth in the Atlantic basin. We show that the primary source of intermodel spread in AMOC weakening arises from changes in the overturning depth. The overturning depth also links the present-day and future AMOC strength. In GCMs with a deeper present-day overturning, the AMOC tends to shoal more under warming because the present-day North Atlantic is less stratified. This allows for greater density changes at depth, which leads to greater AMOC weakening. We use this relation and observations to constrain future AMOC projections and demonstrate that, irrespective of the emission scenario, the AMOC will likely experience only modest weakening over the 21st century.

Controls on Atlantic meridional overturning circulation weakening

The depth-varying transport of the Atlantic basin overturning circulation can be related to the vertical structure of the meridional density gradient through thermal-wind balance[29], which has been shown to provide a good approximation of the AMOC strength in comprehensive GCMs[30–34]. The vertical structure of the density gradient can be decomposed into two factors, representing a characteristic magnitude of the meridional density difference between the high- and low-latitude Atlantic $\Delta_y \rho$ and a characteristic overturning depth H (see Methods). The AMOC strength ψ from thermal-wind balance can then be expressed as

$$\psi = \frac{g}{2\rho_0 f_0}(\Delta_y \rho) H^2, \tag{1}$$

where $g = 9.81\ \mathrm{m\,s^{-2}}$ is the gravitational acceleration, $\rho_0 = 1027.5\ \mathrm{kg\,m^{-3}}$ is a reference density of seawater, and $f_0 = 10^{-4}\ \mathrm{s^{-1}}$ is the Coriolis parameter near 40°N. The two key factors, $\Delta_y \rho$ and H, can be diagnosed directly from CMIP6 output (see Methods). Eq. (1) has previously been shown to provide a good approximation of the present-day AMOC strength in GCMs[34]. By linearizing Eq. (1), the change in AMOC strength $\delta\psi$ can be decomposed as

$$\delta\psi = \frac{g}{2\rho_0 f_0}\left(\underbrace{H^2 \delta(\Delta_y \rho)}_{\text{(A)}} + \underbrace{2(\Delta_y \rho) H \delta H}_{\text{(B)}} + \underbrace{\epsilon}_{\text{(C)}}\right), \tag{2}$$

where (A) represents the AMOC strength change due to a change in $\Delta_y \rho$; (B) represents the AMOC strength change due to a change in H; and (C) represents the residual AMOC strength change due to higher-order terms.

The thermal-wind expression (Eq. 2) captures the AMOC weakening simulated by CMIP6 GCMs at the end of the 21st century. It accounts for approximately 75% of the intermodel variance in AMOC strength changes and exhibits a root-mean-square error of approximately 1 Sv for each emission scenario (Fig. 2a-c).

Furthermore, GCMs that simulate small or large AMOC weakening tend to exhibit small or large AMOC weakening based on thermal-wind balance (Fig. 2).

The ability of the thermal-wind expression to emulate the AMOC weakening in GCMs implies that H and $\Delta_y \rho$ can explain why the present-day AMOC is related to the magnitude of AMOC weakening under warming. Both Term A and Term B can link the present-day AMOC to future AMOC weakening due to their dependence on present-day H and $\Delta_y \rho$ (see Eq. 2). Term B, which represents the AMOC strength change due to δH, is responsible for the majority of the intermodel spread in AMOC weakening, accounting for 74%, 63%, and 61% of the intermodel variance for the SSP1-2.6, SSP2-4.5, and SSP5-8.5 emission scenarios, respectively (hatched bars, Fig. 2a-c). Term B also shows that GCMs with a greater present-day AMOC exhibit greater AMOC weakening. Term A, which represents the AMOC strength change due to $\delta(\Delta_y \rho)$, accounts for a smaller fraction of intermodel variance: 33%, 25%, and 16% for the SSP1-2.6, SSP2-4.5, and SSP5-8.5 emission scenarios, respectively (open bars, Fig. 2a-c). Term A contributes little to the relationship between the present-day and future AMOC strength.

Term B in each individual GCM is similar across the different emission scenarios, indicating that the reason the AMOC weakens similarly across different emission scenarios is due to δH (hatched bars, Fig. 2a-c). Changes in $\Delta_y \rho$ are indeed greater in SSP5-8.5 than in SSP1-2.6, but overall $\delta(\Delta_y \rho)$ does not contribute much to the intermodel spread (open bars, Fig. 2a-c). Given that GCMs with a stronger present-day AMOC tend to exhibit a greater H[34], these results indicate that GCMs with a greater H also have a greater δH under warming.

To understand the processes contributing to δH and its relationship to H, we examine changes to the vertical structure of the Atlantic basin density difference $\Delta_y \rho(z)$, which determines the magnitude of δH (see

Methods). For example, because H depends on the vertically-integrated $\Delta_y\rho(z)$, a small reduction in $\Delta_y\rho$ throughout the water column would lead to more shoaling of H. Conversely, a large reduction in $\Delta_y\rho$ that is confined to the surface ocean would lead to less shoaling of H. Scaling arguments also suggest that H can be linked to the stratification (N^2) of the North Atlantic[34]. A strong present-day North Atlantic N^2 would limit δH by inhibiting the vertical penetration of surface buoyancy flux anomalies that can alter Atlantic basin density. Indeed, we find that GCMs with a weaker present-day AMOC exhibit stronger present-day N^2 in the North Atlantic (40°N–65°N, 50–1000 m; Fig. 3a). The impact of present-day North Atlantic N^2 on $\Delta_y\rho(z)$ change can be seen in vertical profiles of North Atlantic (40°N–65°N) density change, which contributes more to $\Delta_y\rho(z)$ changes when compared to low-latitude (30°S–30°N) Atlantic density changes. Grouping together GCMs with a strong present-day AMOC (red) and a weak present-day AMOC (blue) shows that a strong present-day AMOC and weak present-day North Atlantic N^2 correspond to more vertically uniform North Atlantic density changes. In particular, density changes between 1000 and 2000 m are similar to density changes between 0 and 200 m, consistent with deeper mixing of surface buoyancy flux anomalies (red lines, Fig. 3b-d). Conversely, GCMs with a weak present-day AMOC and strong present-day North Atlantic N^2 tend to exhibit weaker North Atlantic density changes at depth and stronger density changes at the surface, indicating shallower mixing of surface buoyancy flux anomalies (blue lines, Fig. 3b-d).

The results above demonstrate that the present-day North Atlantic N^2 strongly controls vertical density changes in the North Atlantic, which determines the magnitude of AMOC weakening through δH. These results can be summarized by a schematic that depicts GCMs with a weak present-day AMOC (Fig. 4a) and a strong present-day AMOC (Fig. 4b). In GCMs with a weak present-day AMOC, the AMOC tends to be shallow (smaller H) and the North Atlantic tends to be strongly stratified (greater N^2). Under warming, any change to ocean density from surface buoyancy flux anomalies will occur closer to the surface and will not penetrate deeply into the interior of the North Atlantic, leading to weaker density changes at depth. This results in smaller δH and thus smaller AMOC weakening. Conversely, in GCMs with a strong present-day AMOC, the AMOC tends to be deeper (greater H) and the North Atlantic tends to be weakly stratified (smaller N^2). Under warming, the same surface buoyancy flux anomalies will penetrate more deeply into the interior of the North Atlantic, leading to stronger density changes at depth. This results in greater δH and thus greater AMOC weakening.

Constraining Atlantic meridional overturning circulation weakening

We can now leverage this mechanistic understanding of AMOC weakening to constrain AMOC projections over the 21st century (see Methods). The unconstrained probability density function (PDF) of CMIP6 projections suggest that, regardless of the emission scenario, the AMOC most likely will weaken by about 8 Sv at the end of the 21st century (black PDFs, Fig. 5). However, there is considerable intermodel spread, with a high likelihood of even greater AMOC weakening ($\sim$15 Sv).

The previously identified relationship between the present-day and future AMOC strength can be used to constrain AMOC projections by using present-day observations. The AMOC strength diagnosed from the observationally-constrained ECCO state estimate[35] and the linear regression of the present-day AMOC against the future AMOC change (see Methods) suggests that the AMOC will only weaken by about 4 Sv at the end of the 21st century (blue PDFs, Fig. 5). The likelihood of a strong AMOC weakening is substantially reduced, with an AMOC decline greater than 9 Sv being extremely unlikely for all emission scenarios (blue PDFs, Fig. 5).

Can we trust the linear relationship between the present-day and future AMOC strength? Considering that thermal-wind balance accounts for a large portion of the intermodel variance in AMOC weakening, we can examine this assumption by constructing a simple physical expression that links the present-day and future AMOC strength. The AMOC strength change $\delta\psi$ based on thermal-wind can be mainly attributed to δH (Term B in Eq. 2), resulting in

$$\delta\psi \approx \frac{g}{\rho_0 f_0}\overline{(\Delta_y \rho)} H \delta H, \tag{3}$$

where the overline indicates the multi-model mean value of $\Delta_y \rho$, which contributes relatively little to the intermodel spread of the present-day AMOC[34]. Because δH depends on H and $\overline{\Delta_y \rho}$ is a constant, the above expression can related solely to the present-day AMOC strength ψ via regression analysis of H and δH, which results in

$$\delta\psi \approx \frac{g}{\rho_0 f_0}\overline{(\Delta_y \rho)} H(\psi) \left[\alpha_H + \beta_H H(\psi)\right], \tag{4}$$

where a_H is the intercept and b_H is the slope of the linear regression of δH on H. Furthermore, because we have assumed that $\Delta_y \rho$ is a constant, ψ is a function of H only (Eq. 1), enabling us to invert H and make it a function of ψ, which results in

$$H(\psi) = \sqrt{\frac{2\rho_0 f_0 \psi}{g\overline{(\Delta_y \rho)}}}. \tag{5}$$

Eq. (4) predicts $\delta\psi$ solely from ψ via H and thus provides a physical understanding of the statistical relationship between the present-day and future AMOC strength in GCMs.

The physical expression (Eq. 4) describes the AMOC weakening in GCMs slightly more accurately than the linear regression of future AMOC change based on the present-day AMOC strength (compare orange and blue lines, Fig. 5). Eq. (4) better captures the greater AMOC weakening simulated by GCMs with a stronger present-day AMOC because $\delta\psi$ depends non-linearly on H. Using the PDF of observed AMOC strength from ECCO with the prediction of $\delta\psi$ from Eq. (4) (see Methods) gives a further refined estimate of future AMOC weakening (orange PDFs, Fig. 5). The constrained estimate also suggests that the AMOC will weaken by about 4 Sv by 2071–2100 under all emission scenarios. Importantly, for SSP5-8.5, greater AMOC weakening is even less likely with this constraint than based on the linear relationship (compare blue and orange PDFs, Fig. 5c).

These results show that because GCMs simulate a stronger present-day AMOC relative to observations, GCMs also simulate excessive AMOC weakening over the 21st century. This emergent constraint, which we predict from a simple physical expression, corrects these biases and implies that we can expect modest AMOC weakening over the 21st century.

Implications for 21st-century climate projections

In recent years, several studies have raised concerns about a potential collapse of the AMOC in the 21st century[36–38]. These studies argue that independent proxies for the AMOC strength indicate either bi-stable AMOC states or early warnings of AMOC instability in the present climate. However, it has also been argued that some of these studies, particularly those employing statistical models[37], may produce false alarms of AMOC collapse due to artificial increases in variance[39]. While our study does not directly investigate indicators of AMOC collapse, our findings suggest an AMOC collapse during the 21st century is unlikely. In fact, our approach, which uses a physically based relation instead of a statistical model, suggests that AMOC weakening over the 21st century, as simulated by contemporary GCMs, will be modest.

One reason why our conclusions imply modest AMOC weakening could be that contemporary GCMs suffer from a freshwater transport bias that favors a stable AMOC in the present-day climate[36,40,41]. This model bias also affects the stratification of the Atlantic basin and thus H. Ref. 36 corrected this freshwater transport bias in a comprehensive GCM and showed that the AMOC would eventually collapse, although this occurred a few centuries after the abrupt forcing, suggesting no imminent collapse in the 21st century. Furthermore, it has been argued that the freshwater transport criteria does not accurately describe ocean circulation behavior in GCMs[42], casting doubt on the usefulness of freshwater transport as an indicator of a possible AMOC collapse. While recent work has found evidence of AMOC bi-stability in comprehensive GCMs[43–45], these results depend on large freshwater forcing, which is not expected to occur during the 21st century. Additionally, 21st-century AMOC weakening has been mainly attributed to surface heat flux changes[21,46], calling into question the usefulness of examining the potential for a 21st-century AMOC collapse through freshwater hosing experiments.

The key takeaway of this work is that a physically based constraint implies the AMOC will undergo modest weakening over the 21st century. This constraint is relatively independent of the magnitude of greenhouse gas forcing, and explains why AMOC projections over the 21st century are similar for GCMs across different emission scenarios: the present-day Atlantic basin stratification largely determines the degree of AMOC weakening in the 21st century. This indicates that uncertainty in 21st-century AMOC projections is primarily related to intermodel differences in the present-day ocean state rather than the emission scenario. This study adds to a growing body of work that indicates the behavior of the ocean under transient climate change is closely tied to the background ocean state[25,47,48]. Therefore, improving the representation of processes that determine the present-day ocean state will also likely improve future climate projections.

Methods

CMIP6 output This analysis includes all CMIP6 models[20] from the r1i1p1f1 variant label that provide monthly output of ocean potential temperature (thetao), ocean absolute salinity (so), and the meridional overturning streamfunction (msftmz or msftmy) for historical, SSP1-2.6, SSP2-4.5, and SSP5-8.5 emission scenarios. Model names are provided in Figures 1–3. The present-day climatological time period is 1981–2010, and the SSP climatological time period is 2071–2100. The AMOC strength is defined as the maximum value of the meridional overturning streamfunction in the Atlantic basin northward of 30°S and below 500 m. The choice of 500 m avoids volume flux contributions associated with the subtropical ocean gyres. Ocean potential density is calculated from ocean potential temperature and ocean absolute salinity and referenced to 2000 dbar using the Gibbs SeaWater Oceanographic Toolbox of TEOS-10[49]. The Brunt-Väisälä frequency N^2 is calculated from ocean potential density ρ as

$$N^2 = -\frac{g}{\rho_0}\frac{\partial \rho}{\partial z}, \tag{6}$$

and used to indicate stratification of the North Atlantic (40°N–65°N, 50–1000 m).

Observations Observational estimates of the AMOC strength are obtained from the ECCOV4r3 (ECCO) state estimate[35]. ECCO is based on the MITgcm ocean model[50] at 1° resolution with 50 vertical levels. The state estimate is iteratively improved by modifying ocean model initial conditions, parameters, and atmospheric boundary conditions to minimize model-observation disagreement. ECCO output is used to calculate the maximum value of the meridional overturning streamfunction in the Atlantic basin, which is consistent with the definition of the AMOC strength in CMIP6 models. The observed AMOC strength can also be estimated from the Rapid Meridional Overturning Circulation (RAPID) mooring array[51], which was deployed in 2004 to continuously monitor the meridional overturning circulation in the Atlantic basin at 26.5°N. However, this estimate of the AMOC strength is inconsistent with our definition of the AMOC strength from CMIP6 GCMs. A previous study showed that the AMOC strength from ECCO at 26.5°N is in good agreement with the RAPID array[52], which indicates that ECCO provides a suitable estimate of the observed AMOC strength. The annual-mean AMOC strength from ECCO is calculated over the period

1992–2015 and has a mean and standard deviation of 15.3 Sv and 1.2 Sv, respectively.

Thermal-wind expression The thermal-wind expression (Eq. 1) approximates the AMOC strength as a function of the Atlantic basin meridional density difference ($\Delta_y \rho$) and overturning depth (H) under an assumption of mass conservation between zonal and meridional volume transport[29]. The two terms, $\Delta_y \rho$ and H, are diagnosed from CMIP6 ouput. Building on efforts by Ref. 30 and Ref. 34, we estimate $\Delta_y \rho$ and H from the ocean potential density in the Atlantic basin. The term $\Delta_y \rho$ is calculated as the vertical average of the difference in potential density between the North Atlantic (area-averaged from 40°N to 65°N) and the low-latitude Atlantic (area-averaged from 30°S to 30°N) over the upper 2000 m of the Atlantic basin. This estimate of $\Delta_y \rho$ represents the magnitude of the meridional density gradient in the upper cell. The depth H is calculated as the depth where the depth-integrated $\Delta_y \rho$ (for the same regional domains) equals the vertical mean of the depth-integrated $\Delta_y \rho$. This estimate of H is approximately the depth of maximum zonal volume transport[30], and assuming weak eastern boundary currents, can be thought of as the depth of maximum meridional volume transport.

Emergent constraint analysis To obtain a constrained PDF of the change in the AMOC strength $\delta\psi$ for the years 2071–2100, we first calculate a PDF of the observed AMOC strength ψ using ECCO (see subsection above). We assume the PDF of ψ is Gaussian,

$$P\left(\psi\right) = \frac{1}{\sqrt{2\pi\sigma_\psi^2}} \exp\left\{-\frac{\left(\psi - \bar{\psi}\right)^2}{2\sigma_\psi^2}\right\}, \tag{7}$$

where $\bar{\psi}$ is the mean and σ_ψ is the standard deviation of the observed AMOC strength. We then create a constrained PDF of $\delta\psi$ by combining the PDF of the observed AMOC strength $P(\psi)$ and the PDF of the emergent constraint relationship, which estimates $\delta\psi$ given ψ. The emergent constraint PDF is

$$P\left\{\delta\psi|\psi\right\} = \frac{1}{\sqrt{2\pi\sigma_f^2}} \exp\left\{-\frac{\left(\delta\psi - f\left(\psi\right)\right)^2}{2\sigma_f^2}\right\}, \tag{8}$$

where σ_f is the prediction error of the regression and $f(\psi)$ estimates $\delta\psi$ based on ψ (which is described in more detail below). Given these two PDFs, $P(\psi)$ and $P\{\delta\psi|\psi\}$, the PDF for $\delta\psi$ is calculated by numerically integrating

$$P(\delta\psi) = \int_{-\infty}^{\infty} P\{\delta\psi|\psi\}\, P(\psi)\, d\psi. \tag{9}$$

In Eq. (8), $f(\psi)$ is estimated in two separate ways. The first estimate of $f(\psi)$ comes from a linear regression of ψ and $\delta\psi$ based directly on CMIP6 output. This results in

$$f(\psi) = a_\psi + b_\psi \psi, \tag{10}$$

where a_ψ is the intercept and b_ψ is the slope of the linear regression of $\delta\psi$ on ψ. The second estimate of $f(\psi)$ comes from the physical expression introduced in this study, which approximates $\delta\psi$ through Eq. (4).

1. Schmittner, A., Latif, M. & Schneider, B. Model projections of the North Atlantic thermohaline circulation for the 21st century assessed by observations. *Geophysical Research Letters* **32** (2005).

2. Cheng, W., Chiang, J. C. & Zhang, D. Atlantic meridional overturning circulation (AMOC) in CMIP5 models: RCP and historical simulations. *Journal of Climate* **26**, 7187–7197 (2013).

3. Reintges, A., Martin, T., Latif, M. & Keenlyside, N. S. Uncertainty in twenty-first century projections of the Atlantic Meridional Overturning Circulation in CMIP3 and CMIP5 models. *Climate Dynamics* **49**, 1495–1511 (2017).

4. Weijer, W., Cheng, W., Garuba, O. A., Hu, A. & Nadiga, B. CMIP6 models predict significant 21st century decline of the Atlantic meridional overturning circulation. *Geophysical Research Letters* **47**, e2019GL086075 (2020).

5. Buckley, M. W. & Marshall, J. Observations, inferences, and mechanisms of the Atlantic Meridional Overturning Circulation: A review. *Reviews of Geophysics* **54**, 5–63 (2016).

6. Ganachaud, A. & Wunsch, C. Large-scale ocean heat and freshwater transports during the World Ocean Circulation Experiment. *Journal of Climate* **16**, 696–705 (2003).

7. Zhang, R. & Delworth, T. L. Impact of Atlantic multidecadal oscillations on India/Sahel rainfall and Atlantic hurricanes. *Geophysical research letters* **33** (2006).

8. Zhang, R. *et al.* A review of the role of the Atlantic meridional overturning circulation in Atlantic multidecadal variability and associated climate impacts. *Reviews of Geophysics* **57**, 316–375 (2019).

9. Mahajan, S., Zhang, R. & Delworth, T. L. Impact of the Atlantic meridional overturning circulation (AMOC) on Arctic surface air temperature and sea ice variability. *Journal of Climate* **24**, 6573–6581 (2011).

10. Day, J. J., Hargreaves, J., Annan, J. & Abe-Ouchi, A. Sources of multi-decadal variability in Arctic sea ice extent. *Environmental Research Letters* **7**, 034011 (2012).

11. Frierson, D. M. *et al.* Contribution of ocean overturning circulation to tropical rainfall peak in the Northern Hemisphere. *Nature Geoscience* **6**, 940–944 (2013).

12. Schneider, T., Bischoff, T. & Haug, G. H. Migrations and dynamics of the intertropical convergence zone. *Nature* **513**, 45–53 (2014).

13. Marshall, J., Donohoe, A., Ferreira, D. & McGee, D. The ocean's role in setting the mean position of the Inter-Tropical Convergence Zone. *Climate Dynamics* **42**, 1967–1979 (2014).

14. Yin, J., Griffies, S. M. & Stouffer, R. J. Spatial variability of sea level rise in twenty-first century projections. *Journal of Climate* **23**, 4585–4607 (2010).

15. Gregory, J. M. *et al.* The Flux-Anomaly-Forced Model Intercomparison Project (FAFMIP) contribution to CMIP6: Investigation of sea-level and ocean climate change in response to CO 2 forcing. *Geoscientific Model Development* **9**, 3993–4017 (2016).

16. Saenko, O. A., Yang, D. & Myers, P. G. Response of the North Atlantic dynamic sea level and circulation to Greenland meltwater and climate change in an eddy-permitting ocean model. *Climate Dynamics* **49**, 2895–2910 (2017).

17. Vellinga, M. & Wood, R. A. Impacts of thermohaline circulation shutdown in the twenty-first century. *Climatic Change* **91**, 43–63 (2008).

18. Jackson, L. *et al.* Global and European climate impacts of a slowdown of the AMOC in a high resolution GCM. *Climate dynamics* **45**, 3299–3316 (2015).

19. Liu, W., Fedorov, A. V., Xie, S.-P. & Hu, S. Climate impacts of a weakened Atlantic Meridional Overturning Circulation in a warming climate. *Science Advances* **6**, eaaz4876 (2020).

20. Eyring, V. *et al.* Overview of the Coupled Model Intercomparison Project Phase 6 (CMIP6) experimental design and organization. *Geoscientific Model Development* **9**, 1937–1958 (2016).

21. Gregory, J. *et al.* A model intercomparison of changes in the Atlantic thermohaline circulation in response to increasing atmospheric CO2 concentration. *Geophysical Research Letters* **32** (2005).

22. Gregory, J. M. & Tailleux, R. Kinetic energy analysis of the response of the Atlantic meridional overturning circulation to CO 2-forced climate change. *Climate dynamics* **37**, 893–914 (2011).

23. Weaver, A. J. *et al.* Stability of the Atlantic meridional overturning circulation: A model intercomparison. *Geophysical Research Letters* **39** (2012).

24. Kostov, Y., Armour, K. C. & Marshall, J. Impact of the Atlantic meridional overturning circulation on ocean heat storage and transient climate change. *Geophysical Research Letters* **41**, 2108–2116 (2014).

25. Winton, M. *et al.* Has coarse ocean resolution biased simulations of transient climate sensitivity? *Geophysical Research Letters* **41**, 8522–8529 (2014).

26. Lin, Y.-J., Rose, B. E. & Hwang, Y.-T. Mean state AMOC affects AMOC weakening through subsurface warming in the Labrador Sea. *Journal of Climate* **36**, 3895–3915 (2023).

27. Hall, A., Cox, P., Huntingford, C. & Klein, S. Progressing emergent constraints on future climate change. *Nature Climate Change* **9**, 269–278 (2019).

28. Jackson, L. & Petit, T. North Atlantic overturning and water mass transformation in CMIP6 models. *Climate Dynamics* **60**, 2871–2891 (2023).

29. Nikurashin, M. & Vallis, G. A theory of the interhemispheric meridional overturning circulation and associated stratification. *Journal of Physical Oceanography* **42**, 1652–1667 (2012).

30. De Boer, A. M., Gnanadesikan, A., Edwards, N. R. & Watson, A. J. Meridional density gradients do not control the Atlantic overturning circulation. *Journal of Physical Oceanography* **40**, 368–380 (2010).

31. Jansen, M. F., Nadeau, L.-P. & Merlis, T. M. Transient versus equilibrium response of the ocean's overturning circulation to warming. *Journal of Climate* **31**, 5147–5163 (2018).

32. Sigmond, M., Fyfe, J. C., Saenko, O. A. & Swart, N. C. Ongoing AMOC and related sea-level and temperature changes after achieving the Paris targets. *Nature Climate Change* **10**, 672–677 (2020).

33. Bonan, D. B., Thompson, A. F., Newsom, E. R., Sun, S. & Rugenstein, M. Transient and equilibrium responses of the Atlantic overturning circulation to warming in coupled climate models: The role of temperature and salinity. *Journal of Climate* **35**, 5173–5193 (2022).

34. Nayak, M. S., Bonan, D. B., Newsom, E. R. & Thompson, A. F. Controls on the strength and structure of the Atlantic meridional overturning circulation in climate models. *Geophysical Research Letters* **51**, e2024GL109055 (2024).

35. Forget, G. *et al.* ECCO version 4: An integrated framework for non-linear inverse modeling and global ocean state estimation. *Geoscientific Model Development* **8**, 3071–3104 (2015).

36. Liu, W., Xie, S.-P., Liu, Z. & Zhu, J. Overlooked possibility of a collapsed Atlantic Meridional Overturning Circulation in warming climate. *Science Advances* **3**, e1601666 (2017).

37. Boers, N. Observation-based early-warning signals for a collapse of the Atlantic Meridional Overturning Circulation. *Nature Climate Change* **11**, 680–688 (2021).

38. Ditlevsen, P. & Ditlevsen, S. Warning of a forthcoming collapse of the Atlantic meridional overturning circulation. *Nature Communications* **14**, 1–12 (2023).

39. Chen, X. & Tung, K.-K. Evidence lacking for a pending collapse of the Atlantic Meridional Overturning Circulation. *Nature Climate Change* **14**, 40–42 (2024).

40. Hofmann, M. & Rahmstorf, S. On the stability of the Atlantic meridional overturning circulation. *Proceedings of the National Academy of Sciences* **106**, 20584–20589 (2009).

41. Jackson, L. C. *et al.* Challenges simulating the AMOC in climate models. *Philosophical Transactions of the Royal Society A* **381**, 20220187 (2023).

42. Gent, P. R. A commentary on the Atlantic meridional overturning circulation stability in climate models. *Ocean Modelling* **122**, 57–66 (2018).

43. Rahmstorf, S. Bifurcations of the Atlantic thermohaline circulation in response to changes in the hydrological cycle. *Nature* **378**, 145–149 (1995).

44. Boulton, C. A., Allison, L. C. & Lenton, T. M. Early warning signals of Atlantic Meridional Overturning Circulation collapse in a fully coupled climate model. *Nature communications* **5**, 5752 (2014).

45. van Westen, R. M., Kliphuis, M. & Dijkstra, H. A. Physics-based early warning signal shows that AMOC is on tipping course. *Science Advances* **10**, eadk1189 (2024).

46. Maroon, E. A., Kay, J. E. & Karnauskas, K. B. Influence of the Atlantic meridional overturning circulation on the Northern Hemisphere surface temperature response to radiative forcing. *Journal of Climate* **31**, 9207–9224 (2018).

47. He, J., Winton, M., Vecchi, G., Jia, L. & Rugenstein, M. Transient climate sensitivity depends on base climate ocean circulation. *Journal of Climate* **30**, 1493–1504 (2017).

48. Newsom, E., Zanna, L. & Gregory, J. Background pycnocline depth constrains future ocean heat uptake efficiency. *Geophysical Research Letters* **50**, e2023GL105673 (2023).

49. McDougall, T. J. & Barker, P. M. Getting started with TEOS-10 and the Gibbs Seawater (GSW) oceanographic toolbox. *SCOR/IAPSO WG127* **127**, 1–28 (2011).

50. Marshall, J., Adcroft, A., Hill, C., Perelman, L. & Heisey, C. A finite-volume, incompressible Navier Stokes model for studies of the ocean on parallel computers. *Journal of Geophysical Research: Oceans* **102**, 5753–5766 (1997).

51. Cunningham, S. A. *et al.* Temporal variability of the Atlantic meridional overturning circulation at 26.5 N. *Science* **317**, 935–938 (2007).

52. Kostov, Y. *et al.* Distinct sources of interannual subtropical and subpolar Atlantic overturning variability. *Nature Geoscience* **14**, 491–495 (2021).

Acknowledgements The authors thank the climate modeling groups for producing and making available their model output, which is accessible at the Earth System Grid Federation (ESGF) Portal (https://esgf-node.llnl.gov/search/cmip6/). D.B.B was supported by the National Science Foundation (NSF) Graduate Research Fellowship Program (NSF Grant DGE1745301). A.F.T. was supported by the David and Lucile Packard Foundation and NSF Award OCE-1756956. T.S. was supported by Schmidt Sciences, LLC. L.Z. was supported by Schmidt Sciences, LLC. K.C.A was supported by NSF Awards OCE-1850900 and AGS-1752796 and a Calvin Professorship in Oceanography.

Competing Interests The authors declare that they have no competing financial interests.

Correspondence Correspondence and requests for materials should be addressed to David B. Bonan (email: dbonan@caltech.edu).

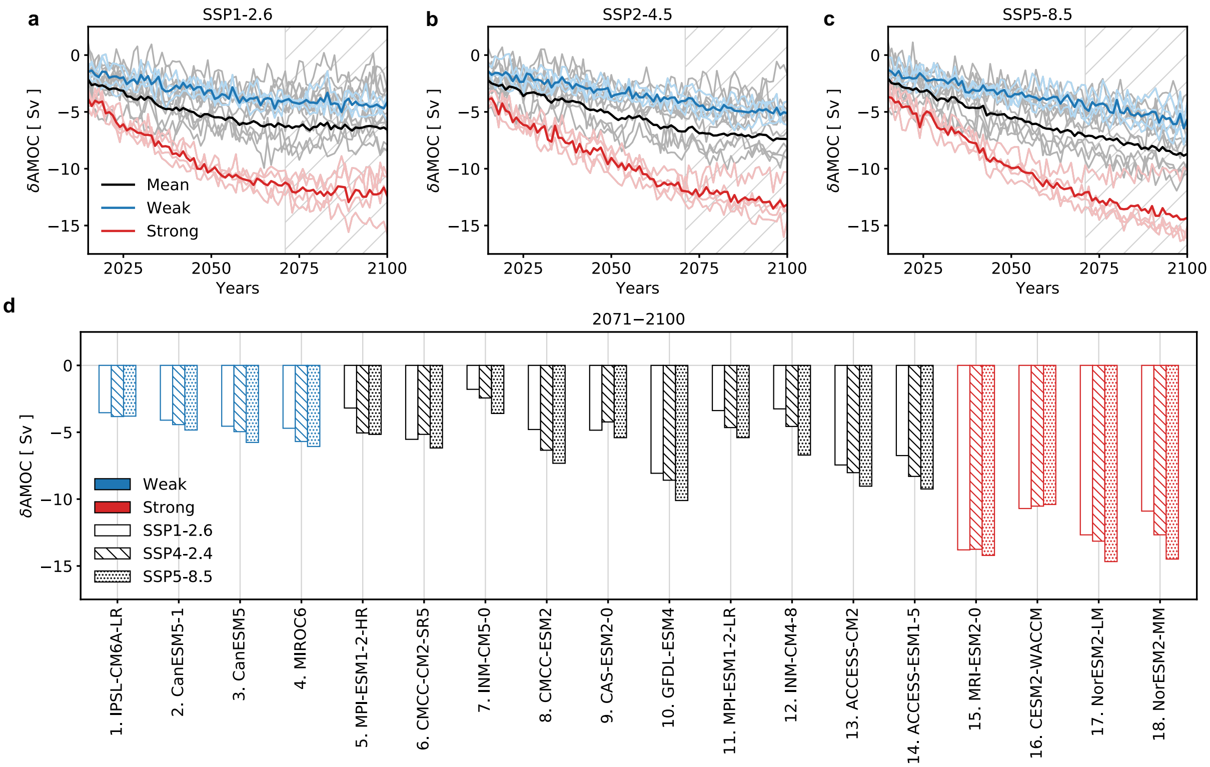

Figure 1: **Relationship between the present-day and future AMOC strength.** Timeseries of the change in AMOC strength for GCMs participating in CMIP6 under (a) SSP1-2.6, (b) SSP2-4.5, and (c) SSP5-8.5 emission scenarios. The thick lines denote the average of the four GCMs with the strongest present-day AMOC (red), the four GCMs with the weakest present-day AMOC (blue), and all other GCMs (black). Each thin line denotes an individual GCM. (d) The change in AMOC strength for GCMs under SSP1-2.6 (open bar), SSP2-4.5 (hatched bar), and SSP5-8.5 (dotted bar) emission scenarios. The present-day time period is 1981–2010 and the SSP time period is 2071–2100, as indicated by the grey hatches in (a-c). GCMs in (d) are ordered from weak to strong present-day AMOC.

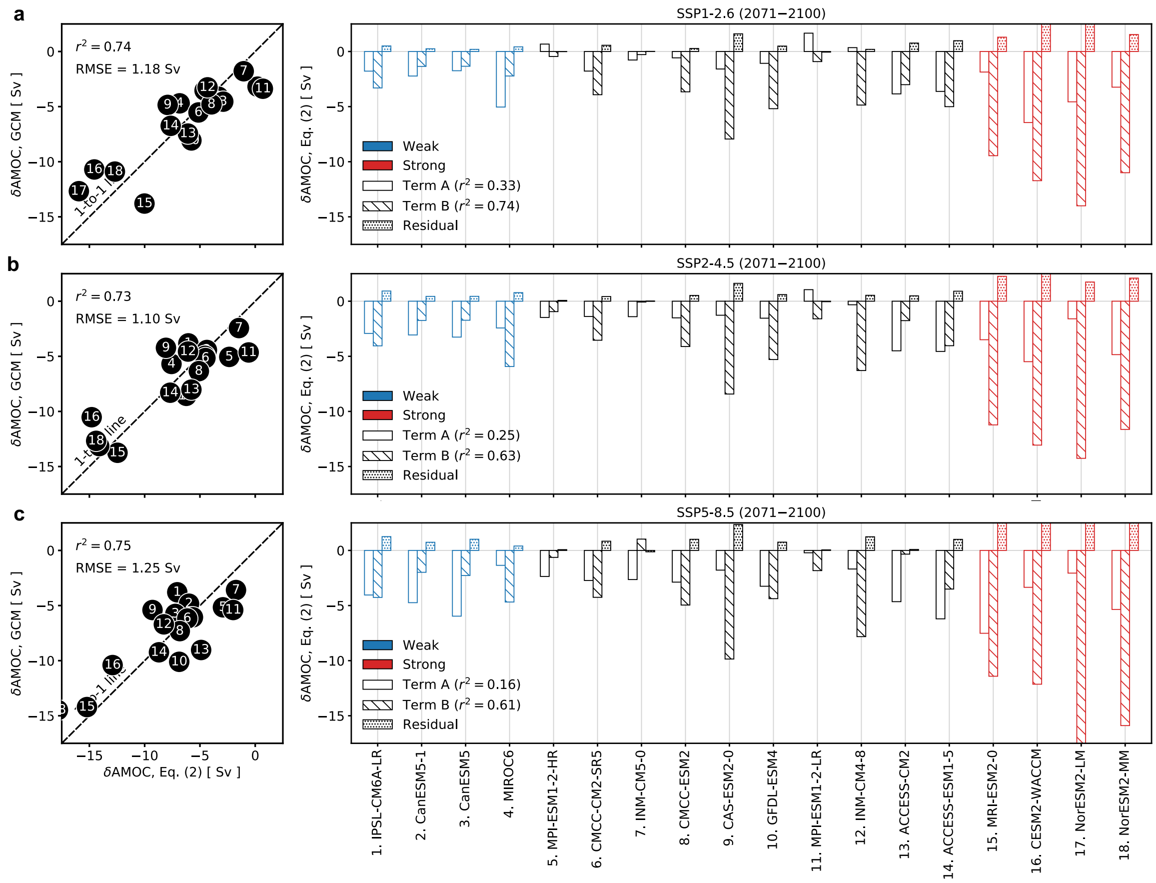

Figure 2: **Controls on AMOC weakening at the end of the 21st century.** Change in the AMOC strength for (a) SSP1-2.6, (b) SSP2-4.5, and (c) SSP5-8.5 emission scenarios. The scatter plots on the left show a comparison of the AMOC strength change predicted by the thermal-wind expression (x-axis) and the AMOC strength change in GCMs (y-axis). The proportion of variance accounted for and root-mean-square error are shown in the top left part of each panel. The bar plots on the right show the AMOC strength change predicted by Term A (white bar), Term B (hatched bar), and the higher-order residual terms (dotted bar) in the thermal-wind expression (Eq. 2). Term A represents changes in the Atlantic basin meridional density difference $\Delta_y \rho$, and Term B represents changes in the overturning depth H. The proportion of variance accounted for by each term is shown in the legend of each panel. The present-day time period is 1981–2010, and the SSP time period is 2070–2100. GCMs are ordered from weak to strong present-day AMOC.

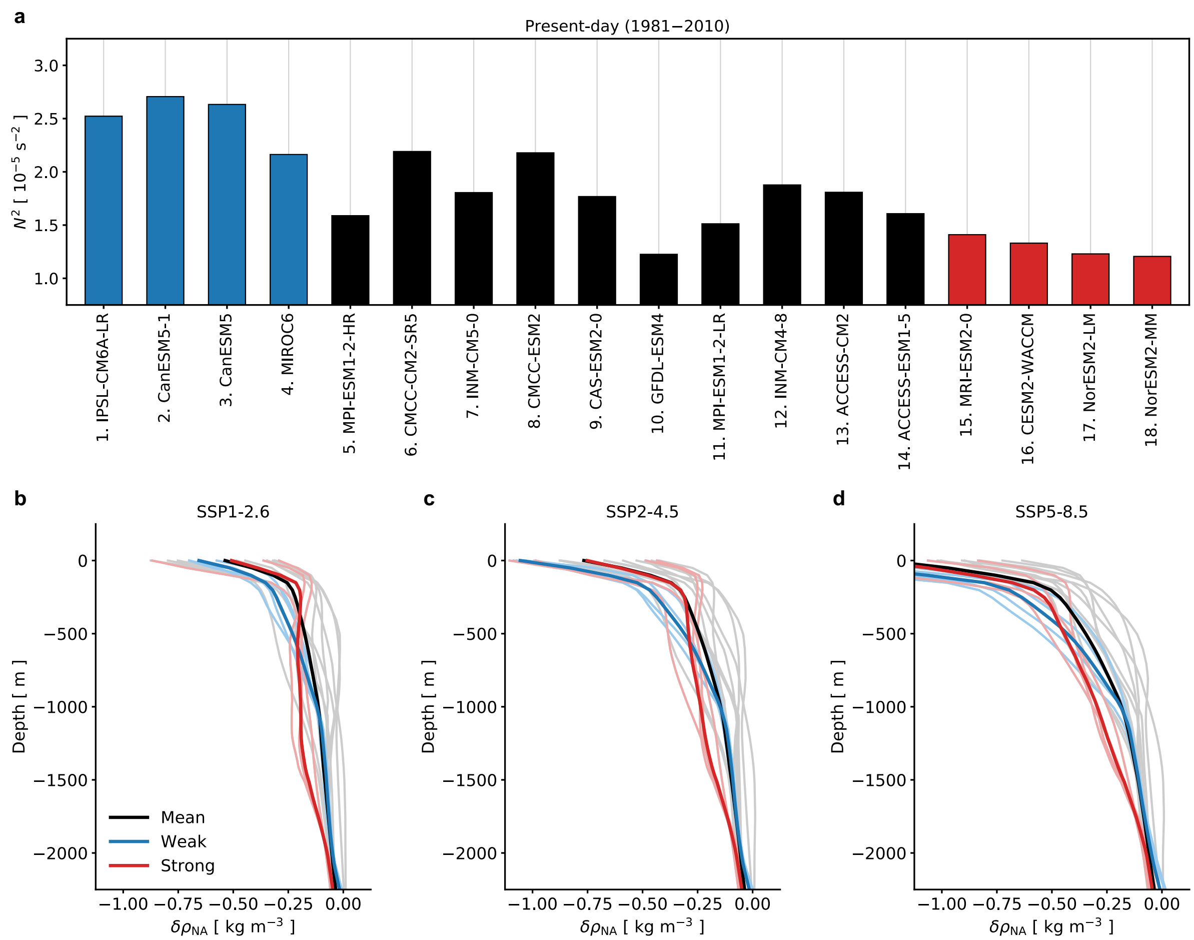

Figure 3: **Relationship between present-day and future North Atlantic stratification.** (a) The present-day stratification (N^2) of the North Atlantic (40°N–65°N, 50–1000 m) from CMIP6 historical simulations. GCMs are ordered from weak to strong present-day AMOC. Change in the North Atlantic density ($\delta\rho_{\mathrm{NA}}$) as a function of depth for (b) SSP1-2.6, (c) SSP2-4.5, and (d) SSP5-8.5 emission scenarios. The present-day time period is 1981–2010 and the SSP time period is 2071–2100. The thick lines denote the average of the four GCMs with the strongest present-day AMOC (red), the four GCMs with the weakest present-day AMOC (blue), and all other GCMs (black). Each thin line denotes an individual GCM.

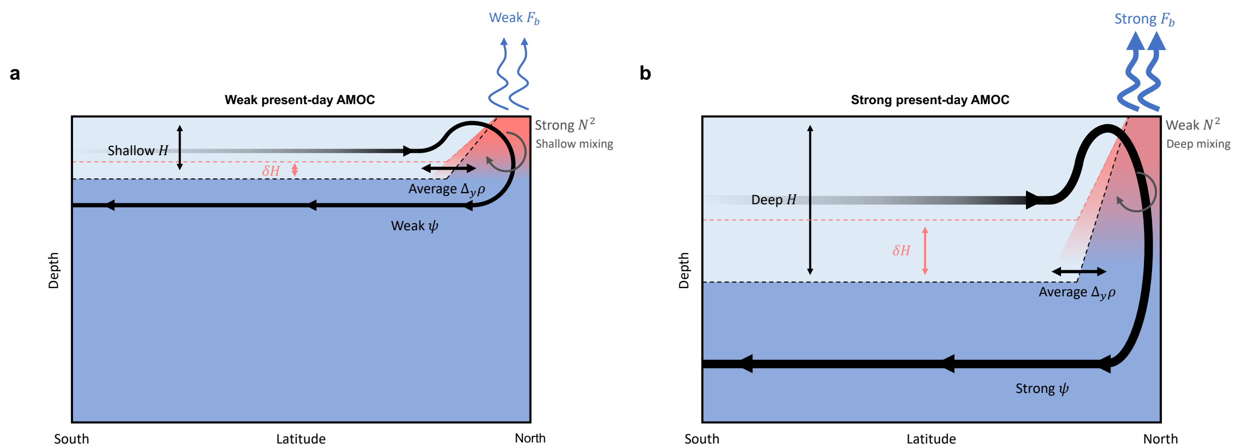

Figure 4: **Schematic depicting controls on the AMOC weakening under warming.** Processes that control the AMOC weakening under warming for GCMs with a (a) weak present-day AMOC and (b) strong present-day AMOC. The dashed line denotes the overturning depth (H). The streamline denotes the meridional overturning streamfunction or AMOC strength (ψ). The blue arrows denote surface buoyancy loss in the North Atlantic (F_b). The grey arrows denote the magnitude of North Atlantic stratification (N^2), which limits mixing deep into the Atlantic basin interior. The black double sided arrows and colors of each isopycnal layer denote the meridional density difference ($\Delta_y\rho$). GCMs with a deeper present-day H tend to have a stronger present-day AMOC and weaker present-day N^2, which enables H to shoal more under warming (as indicated by the red dashed line), resulting in greater AMOC weakening. In other words, a stronger present-day AMOC and weaker present-day N^2 allows for deeper mixing of surface buoyancy flux anomalies into the North Atlantic water column (as indicated by the red shading) and results in greater shoaling and weakening of the AMOC through greater density changes at depth.

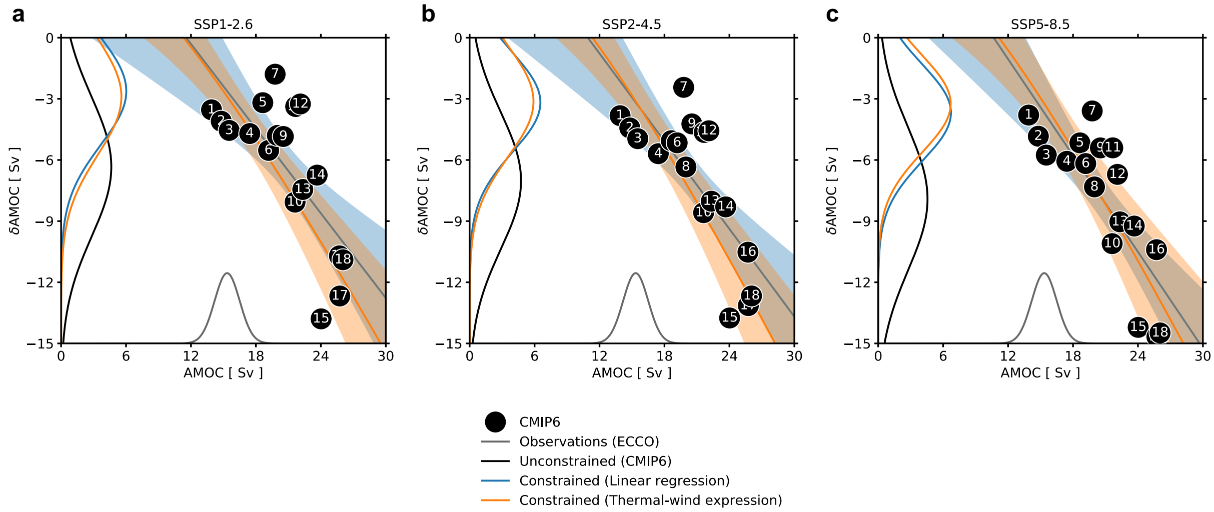

Figure 5: **Constraints on AMOC weakening at the end of the 21st century.** Scatter plot of the present-day (1981–2010) AMOC strength (x-axis) versus the change in AMOC strength (y-axis) under (a) SSP1-2.6, (b) SSP2-4.5, and (c) SSP5-8.5 emission scenarios for years 2071–2100. Each dot denotes a GCM (see Figure 1-3 for model number and model name). The blue line and shading in each panel denotes the linear regression and two standard deviations of the linear regressions, respectively. The orange line in each panel denotes Eq. (4), which predicts the AMOC strength change based on present-day H. The orange shading in each panel denotes the two standard deviations of the linear regressions between H and δH. The grey probability distributions denote observational estimates of the AMOC strength from ECCO. The black probability distributions denote the change in AMOC strength for years 2071–2100 using unconstrained CMIP6 GCMs. The blue probability distributions denote the change in AMOC strength for years 2071–2100 using CMIP6 GCMs constrained by Eq. (4) and observational estimates of the AMOC strength from ECCO. The orange probability distributions denote the change in AMOC strength for years 2071–2100 using CMIP6 GCMs constrained by Eq. (4) and observational estimates of the AMOC strength from ECCO.